AIAA 2016-1826

AIAA SciTech
4-8 January 2016, San Diego, California, USA
54th AIAA Aerospace Sciences Meeting

Adaptive RANS Solution with the High-order Correction Procedure via Reconstruction Method

Lei Shi[*] Cheng Zhou[†] and Z.J. Wang [‡]

Department of Aerospace Engineering, University of Kansas, Lawrence, KS, 66045

In this paper, we present an adjoint-based mesh adaptation method for the Reynolds-averaged Navier-Stokes (RANS) Equations to minimize the output error. A dual-consistent high-order correction procedure via reconstruction method (CPR) is utilized to discretize the RANS equations with the modified Spalart-Allmaras (SA) model. The wall distance of each solution point in the computing domain is computed by solving the Eikonal equation using the CPR framework. The mesh refinements are driven by the automated output-based adaptation. The adaptive results of the turbulence flow over a flat plate problem and the turbulence flow over the NACA0012 airfoil problem demonstrate the ability of the present method to efficiently reduce the functional errors in terms of the number of degrees of freedom (DOFs).

I. Introduction

High-order methods have the potential to achieve higher accuracy at lower cost than lower order methods. This potential has been demonstrated conclusively for smooth problems in several recent International Workshops on High-Order Methods [47]. The use of high-order methods to compute turbulent flows governed by the Reynolds-averaged Navier-Stokes (RANS) equations is an active research topic in the computational fluid dynamics (CFD) community. However, due to the numerical stiffness, the high-order methods for the RANS equations are difficult to converge to the steady-state [35, 37, 38]. For those problems, solution based hp-adaptations offer the best promise. It can ensure the reliability and increase the robustness of the high-order methods for the RANS equations, which has received considerable attentions in the high-order CFD community. [15, 16, 21, 43–45, 52].

In this paper, a dual-consistent high-order correction procedure via reconstruction method (CPR) is utilized to discretize the RANS equations with the modified Spalart-Allmaras (SA) one-equation model. To alleviate the stability issues caused by the negative turbulence working variable, several researchers have proposed a variety of modifications for the SA turbulence model [14, 34, 36]. The modified SA turbulence model investigated in [36] has been demonstrated to significantly improve the robustness of high-order simulations, which is used in the present study. In this model, the r closure function depends on the distance to the nearest wall. To compute the distance of each solution point in the domain to the nearest curved polynomial wall boundaries, the CPR high-order discretization is extended to solve the Eikonal equation.

The effectiveness of adaptive methods highly depends on the accuracy of the error estimation. The dual-weighted residual method proposed by Becker and Rannacher [5] relates a specific functional output directly to the local residual by solving an additional adjoint equation. It can capture the error propagation effects inherent in the hyperbolic equations. This kind of adjoint-based error indicator has been shown very effective in driving a hp-adaptation procedure to obtain a very accurate prediction of the functional outputs [6, 7, 11, 19, 20, 45, 53]. In the present method, a dual-consistent high-order CPR is utilized to compute the discrete adjoint solution associated to the engineer interested outputs, e.g. the lift coefficient, and derive the output-based local error indicator. The mesh refinement procedures are driven by the automated output-based adaptation.

---

[*] Post-doctoral researcher, Department of Aerospace Engineering, 2120 Learned Hall, Lawrence, KS 66045, AIAA Member.

[†] Ph.D. candidate, Department of Aerospace Engineering, 2120 Learned Hall, Lawrence, KS 66045, AIAA Member.

[‡] Spahr Professor and Chair, Department of Aerospace Engineering, 2120 Learned Hall, Lawrence, KS 66045, Associate Fellow of AIAA.

The marked candidate elements for adaptation can be modified by enriching its solution order or subdividing its element or resizing its grid. Thus, the ways to increase the discretization resolution can be generally classified into 3 categories: h-refinement, r-refinement and p-refinement. For h-refinement, subdivision is performed locally for each candidate element to increase the total DOFs. R-refinement or the moving mesh method keeps the total number of nodes the same but moves the location of the grid locally or globally [22]. With p-refinement, the local degree of approximation polynomial is modified. The moving mesh method with curved elements in 3D is till an on-going research. In this work, we only subdivide elements hierarchically for adaptations.

The rest of the paper is organized as follow: In section 2, we briefly review the governing equations and the modified SA model. The high-order CPR formulation and the solution method are presented in Section 3. Section 4 describes the adjoint-based error estimation and the h-adaptation strategies. In Section 5, adaptive results of the turbulence flow over a flat plate problem are presented. Finally, conclusions and some possible future work are given in Section 6.

II. The Modified Spalart-Allmaras Turbulence Model

The compressible RANS equations with the modified one-equation SA turbulence model [14, 34, 36] can be written in the conservative form as

$$\frac{\partial \mathbf{Q}(t)}{\partial t} + \nabla \cdot (\mathbf{F}(\mathbf{Q}) - \mathbf{F_v}(\mathbf{Q}, \nabla \mathbf{Q})) = \mathbf{S}(\mathbf{Q}, \nabla \mathbf{Q}). \tag{1}$$

Here, $\mathbf{Q}$ is the conservative variables , $\mathbf{F}$ is the inviscid flux, $\mathbf{F}_v$ is the viscous flux vector and $\mathbf{S}$ is the source term, which are given by

$$\begin{gathered}
\mathbf{Q} = \begin{pmatrix} \rho \\ \rho u \\ \rho v \\ E \\ \rho\tilde{\nu} \end{pmatrix}, \; \mathbf{F^x} = \begin{pmatrix} \rho u \\ \rho u^2 + P \\ \rho u v \\ u(E+P) \\ \rho u \tilde{\nu} \end{pmatrix}, \; \mathbf{F^y} = \begin{pmatrix} \rho v \\ \rho u v \\ \rho v^2 + P \\ v(E+P) \\ \rho v \tilde{\nu} \end{pmatrix}, \\
\mathbf{F^x_v} = \begin{pmatrix} 0 \\ \tau_{xx} \\ \tau_{xy} \\ u\tau_{xx} + v\tau_{xy} + c_p(\frac{\mu}{Pr} + \frac{\mu_t}{Pr_t})\frac{\partial T}{\partial x} \\ \frac{1}{\sigma}(\mu + \mu\Psi)\frac{\partial \tilde{\nu}}{\partial x} \end{pmatrix}, \; \mathbf{F^y_v} = \begin{pmatrix} 0 \\ \tau_{yx} \\ \tau_{yy} \\ u\tau_{yx} + v\tau_{yy} + c_p(\frac{\mu}{Pr} + \frac{\mu_t}{Pr_t})\frac{\partial T}{\partial y} \\ \frac{1}{\sigma}(\mu + \mu\Psi)\frac{\partial \tilde{\nu}}{\partial y} \end{pmatrix}, \\
\mathbf{S} = \begin{pmatrix} 0 \\ 0 \\ 0 \\ 0 \\ c_{b1}\tilde{S}\rho\nu\Psi + \frac{1}{\sigma}[c_{b2}\rho\nabla\tilde{\nu}\cdot\nabla\tilde{\nu}] - c_{w1}\rho f_w(\frac{\nu\Psi}{d})^2 - \frac{1}{\sigma}\nu(1+\Psi)\nabla\rho\cdot\nabla\tilde{\nu} \end{pmatrix},
\end{gathered} \tag{2}$$

where the ρ, P, E are respectively the density, pressure and specific total energy per unit mass, u,v denote the Cartesian velocity. ν denotes the kinematic viscosity and $\tilde{\nu}$ represents the turbulence working variable of the SA model. Then the pressure P is given by,

$$P = (\gamma - 1)\big(\rho E - \frac{1}{2}\rho(u^2 + v^2)\big), \tag{3}$$

where $\gamma = 1.4$ is the ratio of specific heats. Define velocity vector $\mathbf{u} = (u, v)$, then the fluid viscous stress tensor for Newtonian fluid τ is defined as

$$\tau_{ij} = (\mu + \mu_t)\left(\frac{\partial \mathbf{u}_i}{\partial \mathbf{x}_j} + \frac{\partial \mathbf{u}_j}{\partial \mathbf{x}_i} - \frac{2}{3}\frac{\partial \mathbf{u}_k}{\partial \mathbf{x}_k}\delta_{ij}\right), \tag{4}$$

where δ_{ij} is the Kronecker delta. μ refers to the fluid dynamic viscosity, and μ_t is the turbulence eddy viscosity defined by the SA model reads

$$\begin{aligned} \mu_t &= \begin{cases} \rho\tilde{\nu}f_{v1} & \text{if } \tilde{\nu} \ \geq \ 0 \\ 0 & \text{if } \tilde{\nu} \ < \ 0 \end{cases}. \\ f_{v1} &= \frac{\Psi^3}{\Psi^3 + C_{v1}^3} \end{aligned} \tag{5}$$

For the source term $\mathbf{S}$ of Eq. (2), the production term of the modified SA model $\tilde{S}$ is given as [36]

$$\begin{aligned} \tilde{S} &= \begin{cases} S \ + \ \hat{S} & \text{if } \hat{S} \ \geq \ -c_{v2}S \\ S \ + \ \frac{S(c_{v2}^2 S + c_{v3}\hat{S})}{(c_{v3}-2c_{v2})S - \hat{S}} & \text{if } \hat{S} \ < \ -c_{v2}S \end{cases} \\ S &= \sqrt{\vec{\omega}\cdot\vec{\omega}} \\ \hat{S} &= \frac{\nu\Psi}{\kappa_t^2 d^2} f_{v2} \\ f_{v2} &= 1 \ - \frac{\Psi}{1 + \Psi f_{v1}} \end{aligned} , \tag{6}$$

where $\vec{\omega} = \nabla \times \mathbf{u}$ is the vorticity vector. The destruction term coefficients are given by

$$\begin{aligned} r &= min\left[\frac{\nu\Psi}{\tilde{S}\kappa_t^2 d^2}, 10\right] \\ g &= r \ + \ c_{w2}(r^6 - r) \ , \\ f_w &= g\left(\frac{1 + c_{w3}^6}{g^6 + C_{w3}^6}\right)^{1/6} \end{aligned} \tag{7}$$

where d denotes the distance to the nearest wall at a specific location. The parameter Ψ is designed for high-order discretization schemes to remove the effects of negative turbulence working variable on the robustness of the turbulence model. This parameter is given as

$$\begin{aligned} \Psi &= \begin{cases} 0.05\ln(1 + e^{20\chi}) & \text{if } \chi \ \leq \ 10 \\ \chi & \text{if } \chi \ > \ 10 \end{cases}. \\ \chi &= \frac{\tilde{\nu}}{\nu} \end{aligned} \tag{8}$$

When $\tilde{\nu}$ goes negative, the parameter Ψ can prevent instabilities by turning off the production, destruction and dissipation terms. Finally, the constants in the modified SA model are given as

$$\begin{aligned} & c_{b1} \ = \ 0.1335, \ c_{b2} \ = \ 0.622, \ \sigma \ = \ 2/3, \ \kappa_t \ = \ 0.41, \ P_r \ = \ 0.72, \ P_r t \ = \ 0.9, \\ & c_{w1} \ = \ c_{b1}/\kappa^2 + (1 + c_{b2})/\sigma, \ c_{w2} \ = \ 0.3, \ c_{w3} \ = \ 2, \ c_{v1} \ = \ 7.1, \ c_{v2} \ = \ 0.7, \ c_{v3} \ = \ 0.9 \end{aligned} \tag{9}$$

III. The CPR Discretization

Eqn.1 is discretized using the correction procedure via reconstruction (CPR) method [23][48]. The CPR formulation has some remarkable properties. The framework is easy to understand, efficient to implement and can recover several well known methods such as the discontinuous Galerkin (DG) [2, 4, 12, 13, 39, 40, 51], the spectral volume method (SV) [32, 46, 50] and the spectral difference methods (SD)[27, 30, 31, 33, 42]. For recent development with CPR, interested readers can refer to [9, 10, 17, 18, 24–26, 49, 54].

Assume that the computational domain Ω is discretized into N non-overlapping elements $\{V_i\}_{i=1}^N$. And let Q_i be an approximate solution to the analytical solution Q on V_i. The CPR discretization of Eq. (1) for each solution point j of cell i can be expressed as

$$\frac{\partial \mathbf{Q}_{i,j}}{\partial t} + \prod_j(\nabla\cdot\mathbf{F}(\mathbf{Q}_i)) - \prod_j(\nabla\cdot\mathbf{F}^v(\mathbf{Q}_i, \mathbf{R}_i)) + \frac{1}{|V_i|}\sum_{f\in\partial V_i}\sum_l \alpha_{j,f,l}([\mathbf{F}^n]_{f,l} - [\mathbf{F}^{v,n}]_{f,l})S_f = \mathbf{S}(\mathbf{Q}_i, \mathbf{R}_i), \tag{10}$$

$$\mathbf{R}_{i,j} = (\nabla(Q)_i)_j + \frac{1}{|V_i|}\sum_{f\in\partial V_i}\sum_{l}\alpha_{j,f,l}[\mathbf{Q}^{com} - \mathbf{Q}_i]_{f,l}\vec{n}_f S_f, \tag{11}$$

where $\alpha_{j,f,l}$ are the correction coefficients due to the jumps at the flux point l of face f, S_f is the face area, $|V_i|$ is the cell volume, $[\mathbf{F}^n]$ is the inviscid flux jump and $[\mathbf{F}^{v,n}]$ is the viscous flux jump. The inviscid and viscous flux jumps defined as

$$\begin{aligned}[\mathbf{F}^n] &= \mathbf{F}^n_{com} - \mathbf{F}(\mathbf{Q}_i)\cdot\vec{n}\\ [\mathbf{F}^{v,n}] &= \mathbf{F}^v(\mathbf{Q}^{com},\nabla\mathbf{Q}^{com})\cdot\vec{n} - \mathbf{F}^v(\mathbf{Q}_i,\mathbf{R}_i)\cdot\vec{n}^{\cdot}\end{aligned} \tag{12}$$

Here, $\mathbf{Q}^{com}$ and $\nabla\mathbf{Q}^{com}$ are the common solution and the common gradient on each interface respective. $\mathbf{F}^n_{com}$ denotes a numerical flux on the interface. In the current study, we use the Roe Riemann flux to compute the inviscid common flux $\mathbf{F}^n_{com}$ and the Bassi and Rebay (BR2) [3] for the the common solution $\mathbf{Q}^{com}$ and the common gradient $\nabla\mathbf{Q}^{com}$. $\prod$ is the projection operator for the inviscid and viscous flux divergence terms. The Lagrange polynomial approach (LP) [48] is used.

In the SA model, the working variable $\tilde{\nu}$ can have different order of magnitude than the other components of the state. In order to improve the floating point precision, the dynamic scaling of $\tilde{\nu}$ in [Ref] is used. To compute the distance of each solution point in the domain to the nearest curved polynomial wall boundaries, the CPR high-order discretization is extended to solve the Eikonal equation [Ref].

The first order backward Euler scheme is used for the time integration. The system of linear equations is solved using the preconditioned GMRES (Generalized Minimal RESidual) solvers from the PETSc library [1] . The ILU(1) preconditioner and Line-searches are used to speed up the convergence. More solution details can be found in [8].

IV. Adjoint-based Error Estimation and H-adaptation

Adjoint-based error estimation relates a specific functional output directly to the local residuals by the adjoint solution, which can be used to construct a very effective error indicator to drive an adaptive procedure toward any engineering output. Let Q_h denotes an approximate solution to the analytical solution Q. The difference between them can be interpreted as a solution perturbation $\delta Q = Q - Q_h$. The output error defined as $\delta\mathcal{J} = \mathcal{J}(Q_h) - \mathcal{J}(Q)$ can be estimated by the adjoint weighted residual method

$$\delta\mathcal{J} \approx -\int_\Omega \psi(\mathcal{N}(Q_h) - \mathcal{N}(\mathrm{Q}))\mathrm{d}\Omega = -\int_\Omega \psi\mathcal{N}(Q_h)\mathrm{d}\Omega. \tag{13}$$

Since the CPR method is not in a variational form, the discrete adjoint formulation for the CPR method utilizes an explicitly defined variational form to obtain the dual-consistent adjoint solution. Assume the adjoint solution belongs to the same space of the primal solution, the adjoint variable ψ_i of cell i can be approximated using the Lagrange basis L_j

$$\psi_i = \sum_j L_j\psi_{i,j}. \tag{14}$$

The discrete adjoint equation for the CPR method reads

$$-\sum_i\sum_j \frac{\partial r_{i,j}}{\partial Q_l}\omega_j|J_{i,j}|\psi_{i,j} = \frac{\partial\mathcal{J}}{\partial Q_l}, \tag{15}$$

where $r_{i,j}$ is a pointwise residual defined on each solution point j of cell i arising from a CPR scheme and ω_j and $|J_{i,j}|$ are the quadrature weight and the element Jacobian at the solution point. More detailed discussion about the dual-consistency of the CPR method can be found in Ref. [41].

Based on Eq. 13, the output error estimate can be expressed as

$$\delta\mathcal{J} \approx -\sum_i\sum_j r_{i,j}(Q_h)\omega_j|J_{i,j}|\psi_{i,j}. \tag{16}$$

Also, we can define a corrected output using the functional error estimate

$$\mathcal{J}_{corr} \equiv \mathcal{J}(Q_h) + \delta\mathcal{J}. \tag{17}$$

From the Eq. 13, the output error can be estimated by performing a quadrature rule as

$$\delta \mathcal{J}_h(Q_h) \approx -\sum_i \sum_j \omega_j |J_{i,j}| \psi_{i,j} r_{i,j}(Q_h^H). \tag{18}$$

The continuous adjoint solution ψ is approximated by solving ψ_h on the finner space through enriching the degree of the solution polynomial. The finer solution Q_h is obtained by performing several steps of GMRES relaxation after prolongating from the coarse solution Q_H

$$Q_h^H = I_h^H Q_H \tag{19}$$

with an injection operator I_h^H. The adjoint-based local error indicator η_i used in this paper is defined by taking an absolution value of the elemental output error contribution

$$\eta_i = |\sum_j \omega_j |J_{i,j}| \left(\psi_h - I_h^H \psi_H\right)_{i,j} r_{i,j}(Q_h^H)|. \tag{20}$$

Here, to achieve a better estimates, the adjoint defect between the coarse level and fine level $\psi_h - I_h^H \psi_H$ is used. For systems of equation, the local error indicators are formed by summing together every component's contribution to the functional error estimate.

The error indicators defined above are used to drive a fixed-fraction anisotropic h-adaptation. In this approach, a certain fraction f of the current elements with the largest local error indicators η are marked for h-refinements. Figure 1 shows the procedure of the adjoint-based h-adaptation for the CPR method. Non-conforming interfaces between cells with different h levels are created during the adaptations. In order to ensure the solution smoothness, only one level difference of h-refinement between neighboring cells are allowed. Special treatment is required when computing the common numerical flux on those non-conforming interfaces with hanging nodes. The "mortar" element method developed by Kopriv[28] is used here. For a non-conforming interface, a "mortar" face is introduced to link the unmatched elements, whose space are always chosen as the higher h or p space of the two sides. First, the solution from the left and right sides of the face are prolongated to the mortar surface by a simple interpolation process (see Figure 2a on the following page). Then, the common flux are computed by solving the Riemann problem on the mortar surface. The last step is to project the common flux on the mortar surface back to the original space. Here, the standard L_2 projection is utilized to preserve the average.

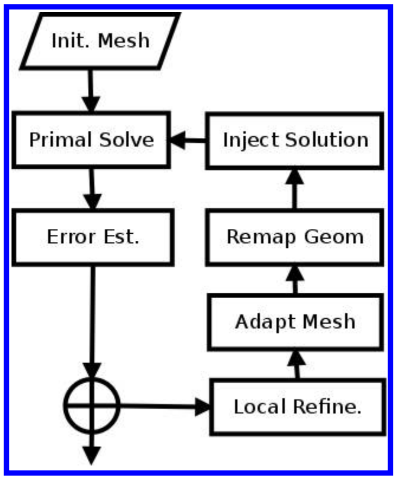

Figure 1: The procedure of the adjoint-based h-adaptation.

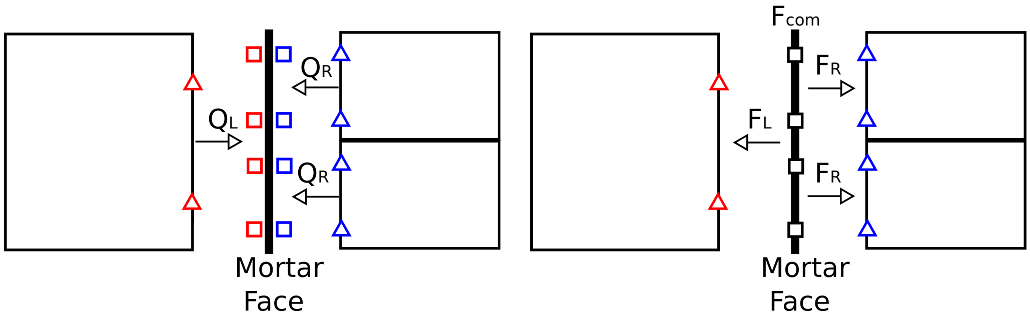

(a) Solution prolongation (b) Common flux restriction

Figure 2: Mortar face operation for a non-conforming face ($k = 1$, △: FPs, □: DOFs on the mortar face).

Mesh refinement is performed in the original element's polynomial space using the reference coordinates. So the refined elements inherit the same geometry approximation order. However, for elements on the geometry boundaries, the newly generated vertex on the boundary edge may not be exactly on the real geometry. An extra remapping process is employed to snap the boundary points to the truth geometry during each adaptation level.

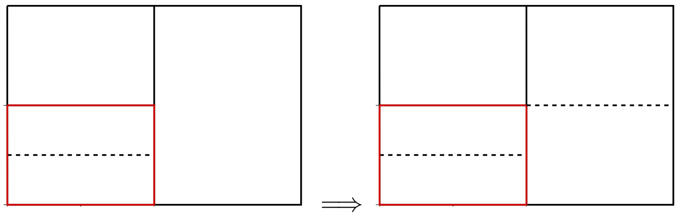

Figure 3: Hanging nodes with the one level difference restriction.

V. Numerical Results

V.A. Turbulence Flow over a Flat Plate

We consider subsonic, turbulence flow over a flat plate. This test case is from the NASA's Turbulence Modeling Resource (TMR) website[29]. The problem is solved on a rectangular domain of size $[-1/3, 2] \times [0, 1]$. The plate length is 2, which spanning from $x = 0.0$ to 2.0. The frees stream Mach number is $M_0 = 0.2$, and the Reynolds number based on the plate length of 1 is $Re = 5 \times 10^6$. The adiabatic no-slip wall boundary condition is enforced along the plate, and a symmetry boundary condition is specified on the first part of the lower boundary. Thus, the leading edge of the plate is a singularity point between the symmetry boundary condition and the no-slip boundary condition. The total pressure and static pressure are fixed respectively on the left and right boundaries. Farfield characteristic boundary condition is enforced on the upper surface. For the laminar viscosity, Sutherland's law with $T_s = 110K$ and $T_{ref} = 300K$ is used.

The 2nd and 3rd order CPR schemes ($k = 1, 2$) with the Gauss points as the SPs/FPs and the LP approach are tested. The initial mesh, as shown in Figure 4a, consists of 34×24 quadrilateral elements, which has an approximate average $y^+ \approx 1.7$ over the plate. In this case, isotropic h-adaptions driven by the drag adjoint error indicator are tested. Figure 4 shows the adapted mesh and the eddy viscosity contours from the finest adaptation stage with $k = 2$. The leading edge and the elements around the lower boundary are refined repeatedly on each adaptation level.

Figure 6a shows the convergence history of the drag coefficient with CFL3D and FUN3D results using the SA model. The results show that the adaptive values converge much faster than the uniform refinements, and all try to converge to the same value. The converged results agree with CFL3D and FUN3D within 0.1

count. The truth $C_D = 0.00285875$ is chosen from the finest $k = 2$ adaptive result. Figure 5 compares the extracted non-dimensional eddy viscosity at $x = 0.97$. The $p = 1$ result shows some oscillations, while the $p = 2$ results shows excellent agreement with the CFL3D and FUN3D results. Figure 6b compares the CD error for all the tested adaptation strategies. With h-adaptation, effective convergence rates of 1.2 and 5.2 were achieved for C_D with $k = 1$ and $k = 2$ respectively, as shown in the Figure 6b. Again it is shown that the ajoint based h-adaptation approach can reduce the number of DOFs by orders of magnitude.

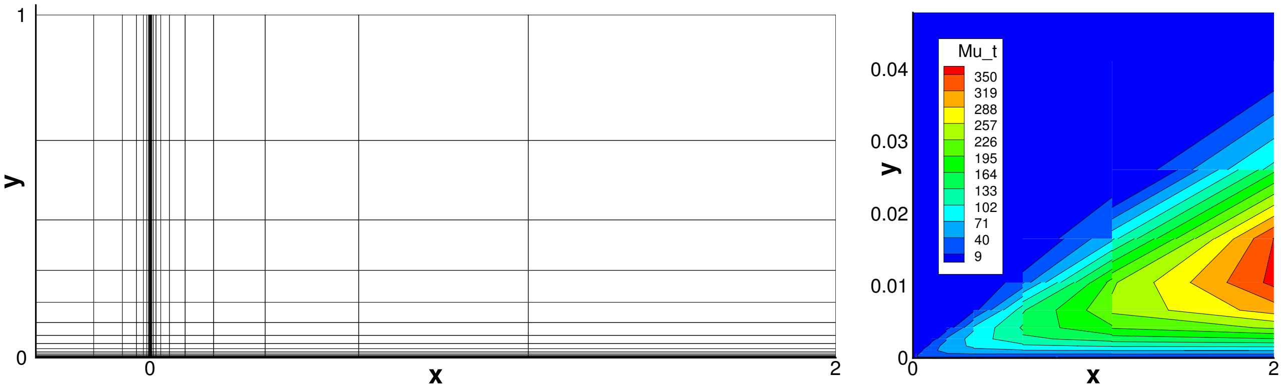

(a) Initial mesh and eddy viscosity contours

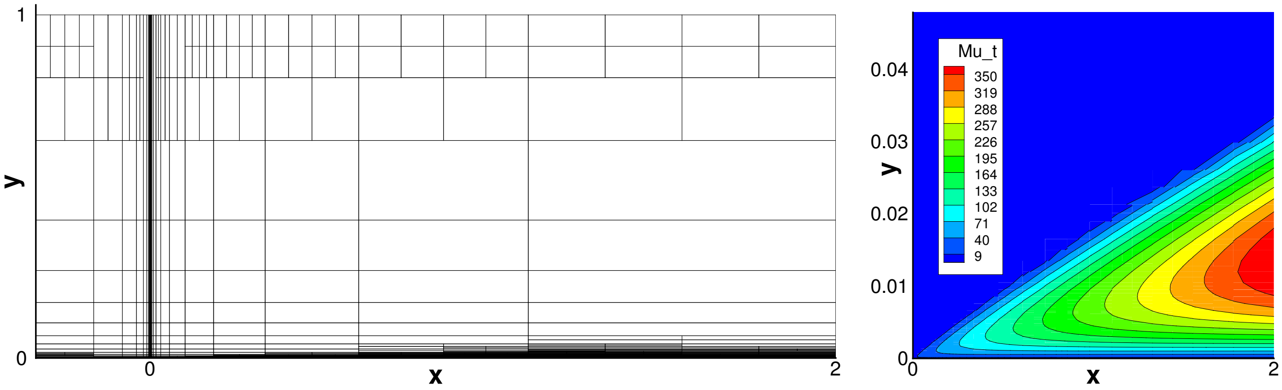

(b) Adapted mesh and eddy viscosity contours

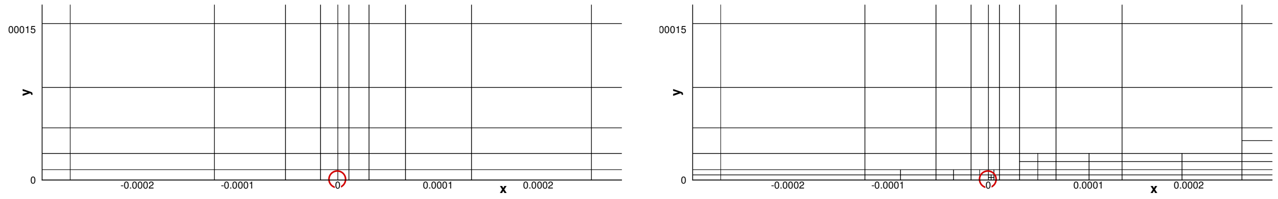

(c) Zoom in, initial mesh

(d) Zoom in, adapted mesh

Figure 4: The initial and adapted results for the turbulence flow ovar a flat plate problem at $M_0 = 0.2$, $Re = 5 \times 10^6 (k = 2)$. Red circle indicates the leading edge.

V.B. Turbulence Flow over the NACA0012 Airfoil

The next test case is a turbulent flow over the NACA0012 airfoil at Mach number Ma=0.15, Reynolds number $Re = 6 \times 10^6$, with angles of attack $\alpha = 0^\circ, 10^\circ$. This case is used as a validation case of CFD codes

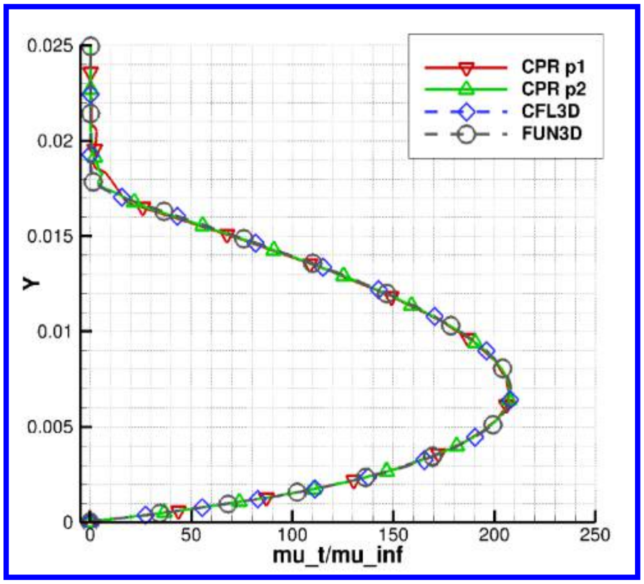

Figure 5: The non-dimensional eddy viscosity of turbulent flow over a flat plate at $Ma = 0.2$, $Re = 5\times10^6$, $x = 0.97$ with 136×96 elements

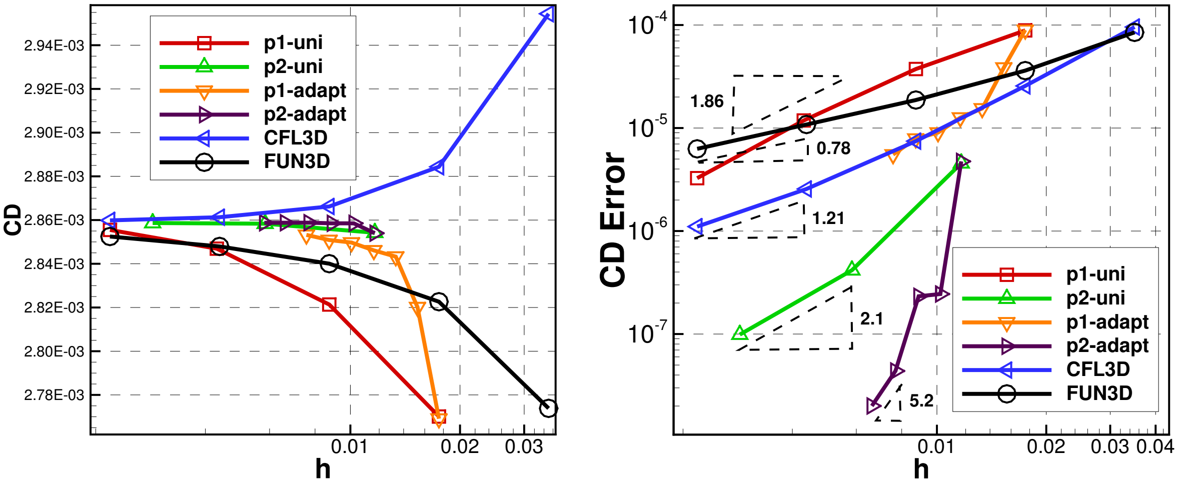

(a) C_D

(b) C_D error

Figure 6: C_D convergence for the turbulent flow over a flat plate problem at $M_0 = 0.2$, $Re = 5 \times 10^6$.

on the TMR webpage[29], by comparing all the CFD results with the experimental results.

The farfield boundary is located almost 500 chords away from the airfoil. The initial mesh is a C-type grid with 54×23 fourth-order curved elements generated using gmsh. The first layer grid gives $y^{+} \approx 10$. H-adaptations with $k = 1, 2, 3, 4$ are driven by the output-based error indicator. The lift coefficient is considered as the outputs of interest. Additionally, uniform h-refinement is performed to compare those adaptation strategies. Figure 7 compares the Mach contours and presents the adapted meshes at angles of attack $\alpha = 0^{\circ}\ and\ 10^{\circ}$. Note that regions near the stagnation streamlines and inside the boundary layer are targeted for refinements. The trailing edge is also refined repeatedly to reduce the effect of the geometry singularity.

Figure 9 displays the convergence history of the drag coefficients along with the CFL3D and FUN3D results. The results show that the adaptive values converge much faster than the uniform refinements, and the adaptation with $k = 3\ and\ 4$ try to converge to the same value between the CFL3D and FUN3D results with much finner grid. The truth outputs is chosen from the the final stage of the adaptive simulations with $k = 4$. Figure 10 compares the C_D errors of all tested adaptation strategies with results from the uniform h-refinements.

VI. Conclusions

In this paper, we apply an output-based h-adaptation method with the high-order CPR formulation to the Reynolds-averaged Navier-Stokes (RANS) Equations to minimize the functional error. A dual-consistent high-order correction procedure via reconstruction method (CPR) is utilized to discretize the RANS equations with the modified Spalart-Allmaras (SA) model. The wall distance of each solution point in the computing domain, which is required in the SA model, is computed by solving the Eikonal equation using the CPR framework. The mesh refinements are driven by the automated output-based adaptation. The adaptive results of the turbulence flow over a flat plate problem and the turbulence flow over the NACA0012 airfoil problem demonstrate the ability of the present method to efficiently reduce the functional errors in terms of the number of degrees of freedom (DOFs).

References

[1] Balay, S., Abhyankar, S., Adams, M. F., Brown, J., Brune, P., Buschelman, K., Dalcin, L., Eijkhout, V., Gropp, W. D., Kaushik, D., Knepley, M. G., McInnes, L. C., Rupp, K., Smith, B. F., Zampini, S., Zhang, H., 2014. PETSc Web page. `http://www.mcs.anl.gov/petsc`.
URL `http://www.mcs.anl.gov/petsc`

[2] Barth, T., Frederickson, P., 1990. Higher order solution of the Euler equations on unstructured grids using quadratic reconstruction. AIAA paper 1990-0013.

[3] Bassi, F., Rebay, S., 1997. A high-order accurate discontinuous finite element method for the numerical solution of the compressible Navier-Stokes equations. Journal of Computational Physics 131 (2), 267–279.

[4] Bassi, F., Rebay, S., 1997. High-order accurate discontinuous finite element solution of the 2D Euler equations. Journal of Computational Physics 138 (2), 251–285.

[5] Becker, R., Rannacher, R., 1996. A feed-back approach to error control in finite element methods: Basic analysis and examples. East-West J. Numer. Math 4, 237–264.

[6] Becker, R., Rannacher, R., 2001. An optimal control approach to a posteriori error estimation in finite element methods. Acta Numerica 10, 1–102.

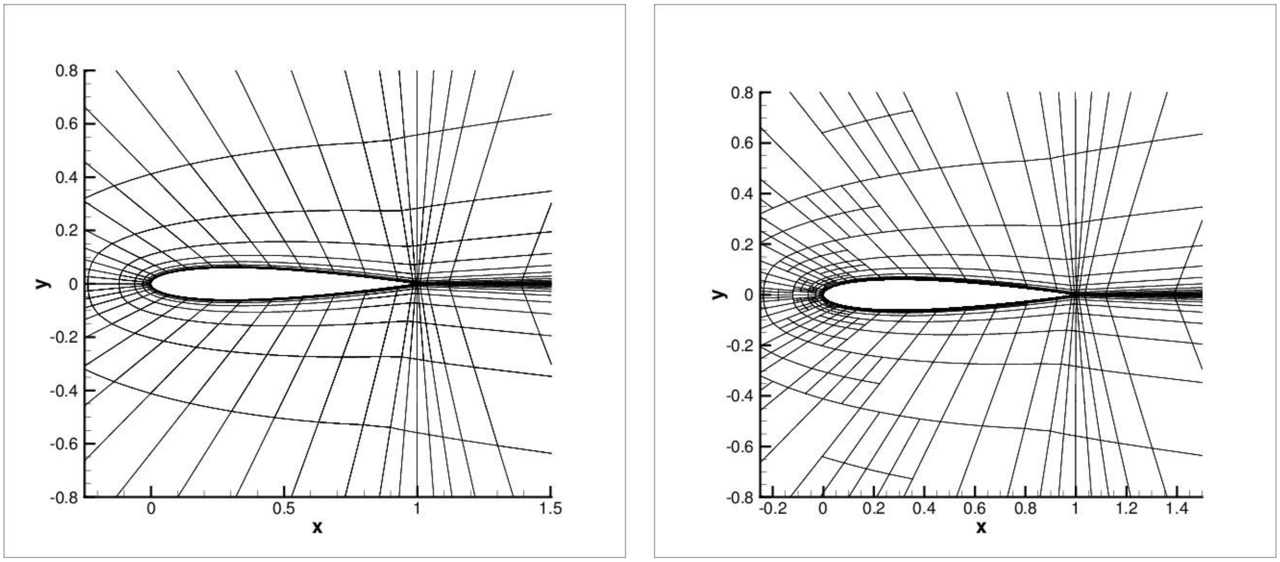

(a) The initial mesh

(b) The adapted mesh

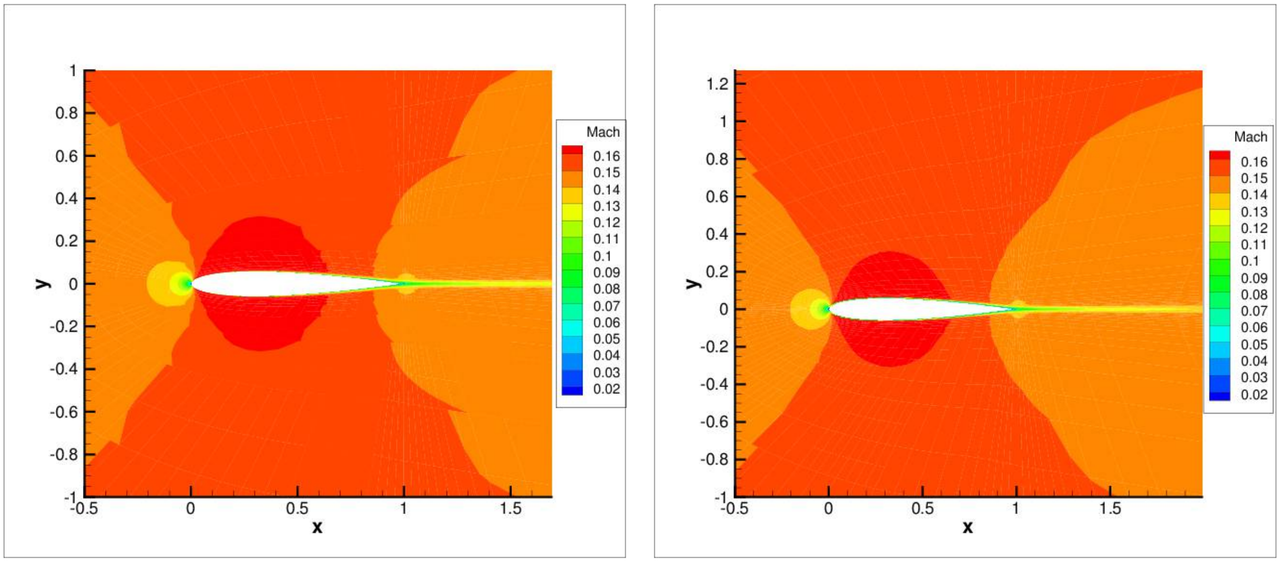

(c) Mach number contours on the initial mesh

(d) Mach number contours on the adapted mesh

Figure 7: Adjoint-based h-adaptation for the NACA 0012 airfoil at $M_0 = 0.15,\ \alpha = 0^\circ,\ Re = 6 \times 10^6$

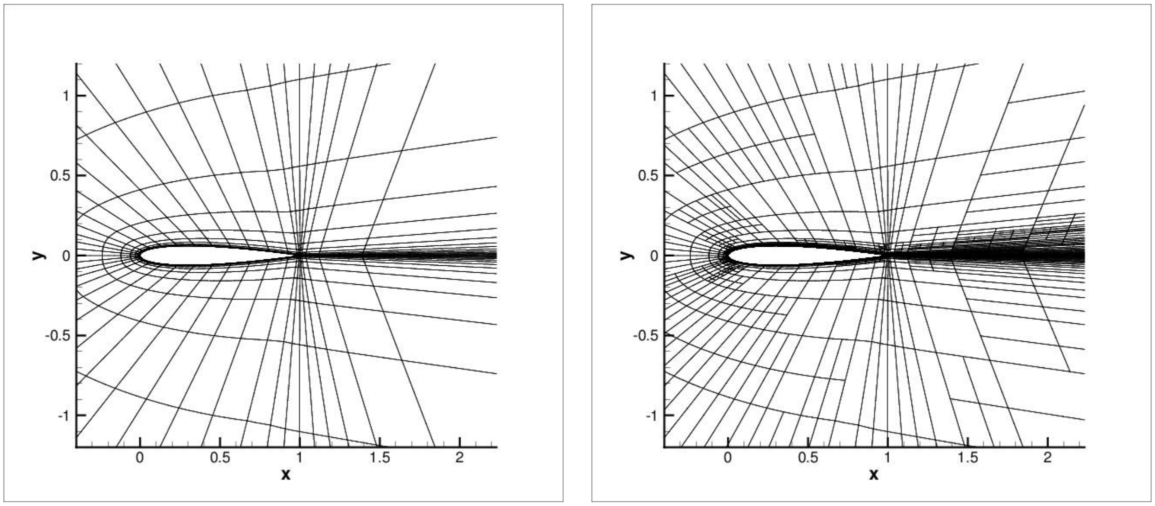

(a) The initial mesh (b) The adapted mesh

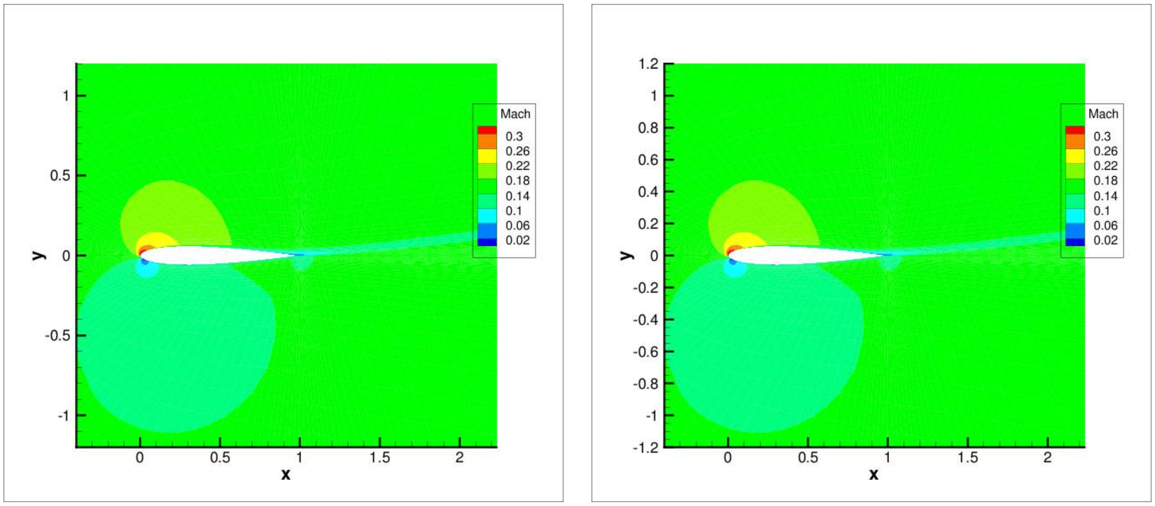

(c) Mach number (the initial mesh) (d) Mach number (the adapted mesh)

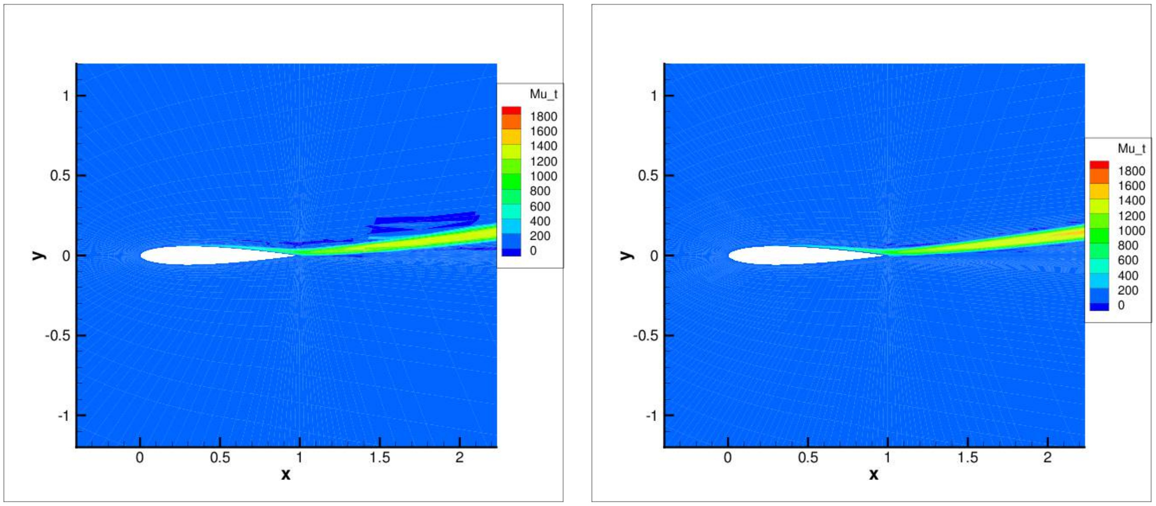

(e) Non-dimensional eddy viscosity (the initial mesh) (f) Non-dimensional eddy viscosity (the adapted mesh)

Figure 8: Adjoint-based h-adaptation for the NACA 0012 airfoil at $M_0 = 0.15,\ \alpha = 10^\circ,\ Re = 6 \times 10^6$

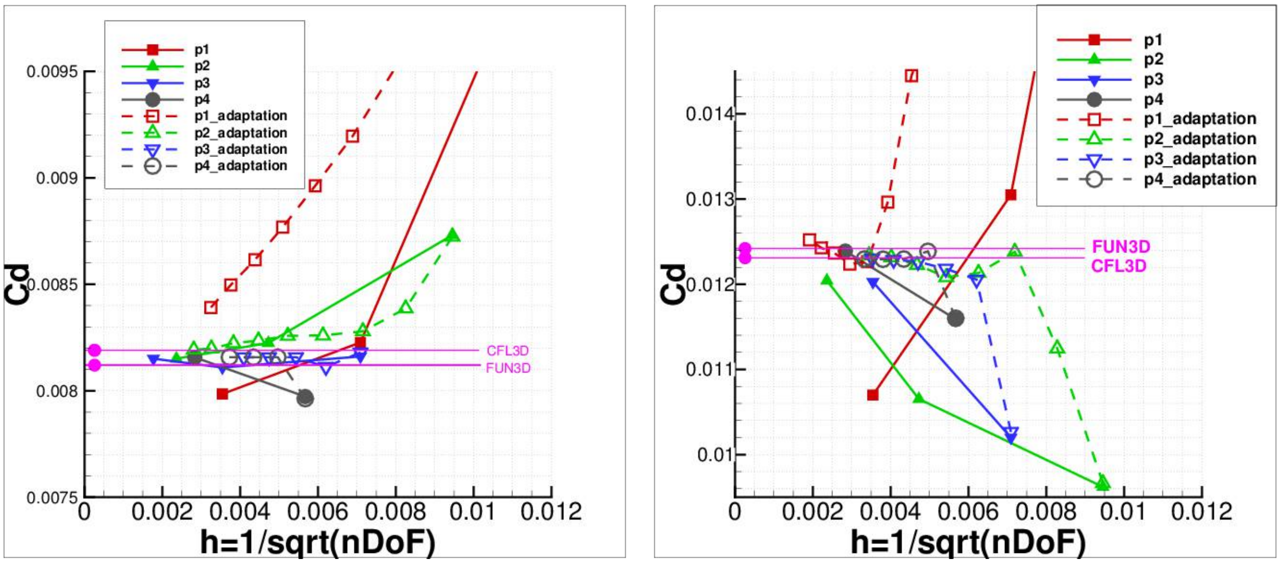

(a) $\alpha = 0^\circ$

(b) $\alpha = 10^\circ$

Figure 9: C_D convergence for turbulence flow over the NACA 0012 airfoil at $M_0 = 0.15,\ \alpha = 1^\circ\ and\ 10^\circ,\ Re = 6\times10^6$

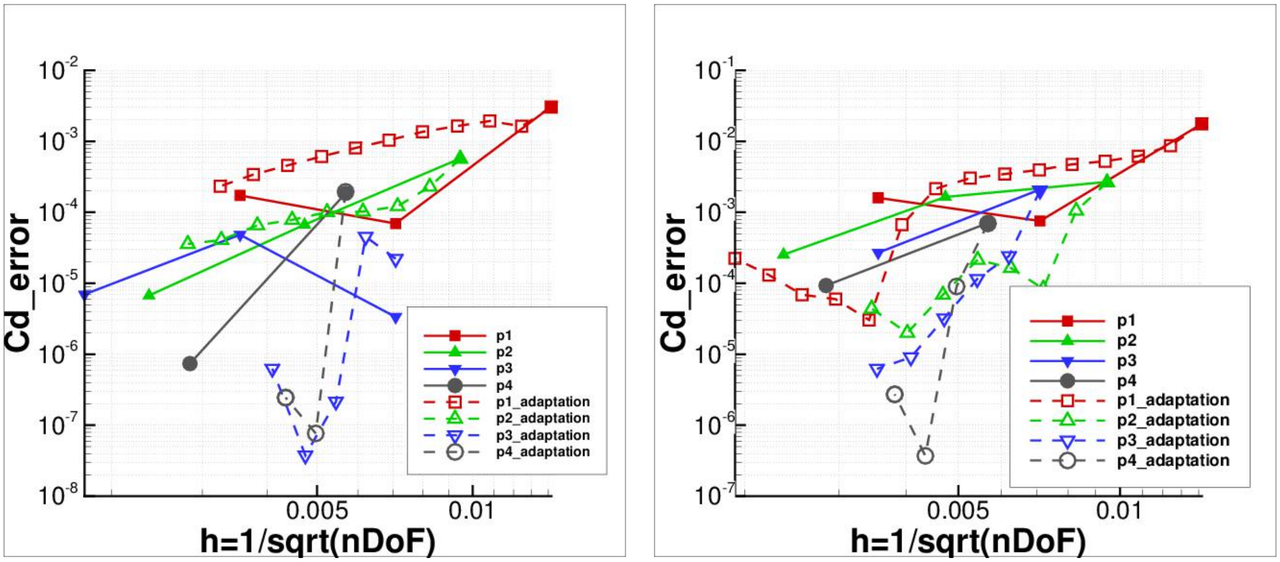

(a) $\alpha = 0^\circ$

(b) $\alpha = 10^\circ$

Figure 10: C_D error for turbulence flow over the NACA 0012 airfoil at $M_0 = 0.15,\ \alpha = 1^\circ\ and\ 10^\circ,\ Re = 6\times10^6$

[7] Burgess, N., 2011. An adaptive discontinuous Galerkin solver for aerodynamic flows. Ph.D. thesis, University of Wyoming.

[8] C. Zhou, Z. J. W., 2015. Cpr high-order discretization of the RANS equations with the SA model. AIAA Paper 2015-1286.

[9] Cagnone, J., Nadarajah, S., 2012. A stable interface element scheme for the p-adaptive lifting collocation penalty formulation. Journal of Computational Physics 231 (4), 1615 – 1634.

[10] Cagnone, J., Vermeire, B., Nadarajah, S., 2013. A p-adaptive LCP formulation for the compressible Navier-Stokes equations. Journal of Computational Physics 233, 324 – 338.

[11] Ceze, M., Fidkowski, K. J., 2012. Anisotropic hp-adaptation framework for functional prediction. AIAA Journal 51 (2), 492–509.

[12] Cockburn, B., Lin, S., Shu, C., 1989. TVB Runge-Kutta local projection discontinuous Galerkin finite element method for conservation laws III: One-dimensional systems. Journal of Computational Physics 84 (1), 90–113.

[13] Cockburn, B., Shu, C., 1998. The Runge-Kutta discontinuous Galerkin method for conservation laws V: Multidimensional systems. Journal of Computational Physics 141 (2), 199–224.

[14] D.Moro, N. N., Peraire, J., 2011. Navier-Stokes solution using hybridizable discontinuous Galerkin methods. AIAA Paper 2011-3407.

[15] Fidkowski, K., 2011. Review of output-based error estimation and mesh adaptation in computational fluid dynamics. AIAA Journal 49 (4), 673–694.

[16] Fidkowski, K., Darmofal, D., 2007. A triangular cut-cell adaptive method for high-order discretizations of the compressible Navier-Stokes equations. Journal of Computational Physics 225 (2), 1653–1672.

[17] Gao, H., Wang, Z. J., Jan. 2013. A conservative correction procedure via reconstruction formulation with the chain-rule divergence evaluation. Journal of Computational Physics 232, 7–13.

[18] Gao, H., Wang, Z. J., 2013. Differential formulation of discontinuous Galerkin and related methods for the Navier-Stokes equations. Commun. Comput. Phys. 13, 1013–1044.

[19] Giles, M., Pierce, N., 1997. Adjoint equations in CFD: duality, boundary conditions and solution behaviour. AIAA paper 97-1850.

[20] Giles, M., Pierce, N., 2003. Adjoint error correction for integral outputs. In: Barth, T., Deconinck, H. (Eds.), Error Estimation and Adaptive Discretization Methods in Computational Fluid Dynamics. Vol. 25 of Lecture Notes in Computational Science and Engineering. Springer Berlin Heidelberg, pp. 47–95.

[21] Hartmann, R., Houston, P., 2002. Adaptive discontinuous Galerkin finite element methods for the compressible Euler equations. Journal of Computational Physics 183 (2), 508 – 532.

[22] Huang, W., Russell, R. D., 2010. Adaptive Moving Mesh Methods. Vol. 174. Springer.

[23] Huynh, H. T., 2007. A flux reconstruction approach to high-order schemes including discontinuous Galerkin methods. AIAA Paper 2007-4079.

[24] Huynh, H. T., 2011. High-order methods by correction procedures using reconstructions. Adaptive High-Order Methods in Computational Fluid Dynamics 2, 391–422.

[25] Huynh, H. T., Z. J. W., Vincent, P. E., 2014. High-order methods for computational fluid dynamics: A brief review of compact differential formulations on unstructured grids. Computers & Fluids 98 (0), 209–220.

[26] Jameson, A., Vincent, P. E., Castonguay, P., Feb. 2012. On the non-linear stability of flux reconstruction schemes. J. Sci. Comput. 50 (2), 434–445.

[27] Kopriva, D., Kolias, J., 1996. A conservative staggered-grid chebyshev multidomain method for compressible flows. Journal of computational physics 125 (1), 244–261.

[28] Kopriva, D. A., 1996. A conservative staggered-grid chebyshev multidomain method for compressible flows. II. a semi-structured method. Journal of Computational Physics 128 (2), 475 – 488.

[29] Lagnley Research Center, 2014. Turbulence modeling resource.
URL `http://turbmodels.larc.nasa.gov/`

[30] Liang, C., Jameson, A., Wang, Z. J., May 2009. Spectral difference method for compressible flow on unstructured grids with mixed elements. Journal of Computational Physics 228 (8), 2847–2858.

[31] Liu, Y., Vinokur, M., Wang, Z. J., 2006. Discontinuous spectral difference method for conservation laws on unstructured grids. Computational Fluid Dynamics 2004, 449–454.

[32] Liu, Y., Vinokur, M., Wang, Z. J., 2006. Spectral finite volume method for conservation laws on unstructured grids V: Extension to three-dimensional systems. Journal of Computational Physics 212 (2), 454–472.

[33] May, G., Jameson, A., 2006. A spectral difference method for the Euler and Navier-Stokes equations on unstructured meshes. AIAA paper 2006-304.

[34] N. K. Burgess, D. J. M., 2012. Robust computation of turbulent flows using a discontinuous Galerkin method. AIAA Paper 2012-0457.

[35] Nicholas K. Burgess, C. R. N., Mavriplis, D. J., 2010. Efficient solution techniques for discontinuous Galerkin discretizations of the Navier-Stokes equations on hybrid anisotropic meshes. AIAA Paper 2010-1448.

[36] Oliver, T. A., 2008. A high-order, adaptive, discontinuous Galerkin finite element method for the Reynolds averaged Navier-Stokes equations. Ph.D. thesis, Massachusetts Institute of Technology.

[37] Oliver, T. A., Darmofal, D. L., 2007. An unsteady adaptation algorithm for discontinuous Galerkin discretizations of the RANS equations. AIAA Paper 2007-914.

[38] Per-Olof Persson, N. C. N., Peraire, J., 2007. RANS solutions using high order discontinuous Galerkin methods. AIAA Paper 2007-914.

[39] Peraire, J., Persson, P., 2007. The compact discontinuous Galerkin CDG method for elliptic problems. Arxiv preprint math/0702353.

[40] Reed, W. H., Hill, T. R., 1973. Triangular Mesh Methods for the Neutron Transport Equation.

[41] Shi, L., Wang, Z. J., 2015. Adjoint-based Error Estimation and Mesh Adaptation for the Correction Procedure via Reconstruction Method. Journal of Computational Physics 295, 261–284.

[42] Van den Abeele, K., Lacor, C., Wang, Z. J., 2008. On the stability and accuracy of the spectral difference method. Journal of Scientific Computing 37 (2), 162–188.

[43] Venditti, D., Darmofal, D., 2003. Anisotropic grid adaptation for functional outputs: application to two-dimensional viscous flows. Journal of Computational Physics 187 (1), 22–46.

[44] Venditti, D. A., Darmofal, D. L., Oct. 2000. Adjoint error estimation and grid adaptation for functional outputs: application to quasi-one-dimensional flow. Journal of Computational Physics 164 (1), 204–227.

[45] Wang, L., Mavriplis, D. J., Nov. 2009. Adjoint-based hp-adaptive discontinuous Galerkin methods for the 2D compressible Euler equations. Journal of Computational Physics 228 (20), 7643–7661.

[46] Wang, Z. J., 2002. Spectral (finite) volume method for conservation laws on unstructured grids: basic formulation. Journal of Computational Physics 178 (1), 210–251.

[47] Wang, Z. J., Fidkowski, K., Abgrall, R., Bassi, F., Caraeni, D., Cary, A., Deconinck, H., Hartmann, R., Hillewaert, K., Huynh, H. T., Kroll, N., May, G., Persson, P.-O., van Leer, B., Visbal, M., Jul. 2013. High-order CFD Methods: Current Status and Perspective. International Journal for Numerical Methods in Fluids 72, 811–845.

[48] Wang, Z. J., Gao, H., 2009. A unifying lifting collocation penalty formulation including the discontinuous Galerkin, spectral volume/difference methods for conservation laws on mixed grids. Journal of Computational Physics 228, 8161–8186.

[49] Wang, Z. J., Gao, H., Haga, T., 2011. A unifying discontinuous formulation for hybrid meshes. Adaptive High-Order Methods in Computational Fluid Dynamics, 423–453.

[50] Wang, Z. J., Liu, Y., 2002. Spectral (finite) volume method for conservation laws on unstructured grids II. extension to two-dimensional scalar equation. Journal of Computational Physics 179 (2), 665–697.

[51] Warburton, T., 2006. An explicit construction of interpolation nodes on the simplex. Journal of engineering mathematics 56 (3), 247–262.

[52] Yang, X., Huang, W., Qiu, J., 2012. A moving mesh weno method for one-dimensional conservation laws. SIAM Journal on Scientific Computing 34 (4), A2317–A2343.

[53] Yano, M., Darmofal, D. L., Sep. 2012. An optimization-based framework for anisotropic simplex mesh adaptation. Journal of Computational Physics 231 (22), 7626–7649.

[54] Yu, M., Wang, Z. J., Liu, Y., 2014. On the accuracy and efficiency of discontinuous Galerkin, spectral difference and correction procedure via reconstruction methods. Journal of Computational Physics 259, 70–95.